

# Cavity dynamics and particle alignment in the wake of a supersonic projectile penetrating a dusty plasma

O. Arp,<sup>\*</sup> D. Caliebe, and A. Piel

*Institut für Experimentelle und Angewandte Physik, Christian-Albrechts-Universität,  
Olshausenstr. 40, D-24098 Kiel, Germany*

(Received 1 December 2010; published 10 June 2011)

The penetration of a projectile into a strongly coupled dusty plasma was studied in a radio-frequency discharge under microgravity conditions. A supersonic projectile produces an elongated dust-free cavity in its wake. The dynamics of the cavity is analyzed and compared with Langevin dynamics simulations. Besides a three-dimensional Mach cone structure, the simulation shows that the cavity dynamics can be subdivided into three phases: An opening phase with fixed time scale, a closing phase, whose duration is affected by the projectile speed and, finally, a phase of particle realignment in the target cloud, which persists for a long time after the closure of the cavity.

DOI: [10.1103/PhysRevE.83.066404](https://doi.org/10.1103/PhysRevE.83.066404)

PACS number(s): 52.27.Lw, 52.35.Tc, 83.10.Rs

## I. INTRODUCTION

The interaction of fast-moving objects (projectiles) with different types of matter have been studied in many different contexts like, e.g., the collision of cometary dust grains with aerogels [1] or the impact of projectiles on water [2], non-Newtonian [3] or colloidal liquids [4], and on granular matter [5]. All these examples show complex dynamical effects, especially the formation of cavities in the wake of the projectile when it deeply penetrates the target. A key for the understanding of the complex dynamical behavior of these cavities is a detailed knowledge of how momentum from the projectile is transferred to and distributed in the target material. Unfortunately, studying these mechanisms on the atomic level in a three-dimensional system is either impossible, in a real solid or liquid, or the lacking transparency of the medium limits the observation to the surface or a boundary layer.

A system that is not affected by these limitations is a dusty (complex) plasma. It is one of the softest types of matter and a unique laboratory for studying dynamical processes in fluid and crystal phases on the quasicrystalline level. A dusty plasma consists of charged, typically micrometer-sized, solid particles (dust) that are levitated in a gas discharge and interact via a screened Coulomb (Yukawa) potential. Since the nearest-neighbor distance is much larger than the particle diameter, dusty plasmas are highly transparent and allow observation of each individual particle even in extended three-dimensional systems. Because gravity usually leads to the formation of flat dust suspensions, the observation of spatially extended three-dimensional dusty plasmas requires suitable measures of gravity compensation [6] or weightlessness conditions [7].

The effect of moving pointlike disturbances was studied extensively in a two-dimensional dusty plasma and showed the formation of V-shaped Mach cone patterns in the wake of a fast particle [8] or behind a disturbance caused by a laser beam [9]. Experimental investigations of isolated projectiles penetrating a three-dimensional dusty plasma are rare and accidental [10]. Usually, the disturbances are relatively weak and lead to only moderate variations of the interparticle

distance. Experiments with a moving tungsten wire in a three-dimensional dusty plasma [11] showed the formation of a teardrop-shaped dust-free cavity in the wake of the wire. Such strong disturbances, which partially destroy the natural structure of the dust cloud, are also expected for large isolated projectiles that move through a dusty plasma. We report on first results from such experiments performed under microgravity conditions on parabolic flights, where we studied the interaction of injected supersonic projectiles and a stationary dusty plasma. The observations are compared with three-dimensional Langevin dynamics simulations.

## II. EXPERIMENTAL SETUP

The experiments were performed in the IMPF-K2 discharge chamber, which is a modification of the device described in Ref. [12] with a simplified electrode setup. The vertical section of the device in Fig. 1 shows a symmetric parallel-plate radiofrequency (rf) discharge with two circular electrodes forming the discharge gap. Two sinusoidal rf voltages of identical amplitude and a frequency  $f_{rf} = 13.56$  MHz were coupled in push-pull mode to the two electrodes. The self-bias of the discharge was suppressed by shunt resistors. The discharge was operated in argon at a pressure of  $p = 30$  Pa and rf voltages of  $U_{rf} = 65V_{pp}$ . Monodisperse spherical melamine formaldehyde (MF) particles of  $r_t = 4.8$   $\mu\text{m}$  radius were injected into the discharge to form the target cloud. Fast projectiles were generated in a dust accelerator device (Fig. 1), which used an electromechanically agitated dust dispenser to drop a shower of monodisperse spherical polymethyl methacrylate (PMMA) particles of  $r_p = 10$   $\mu\text{m}$  radius onto a spinning (2036 rpm) cogwheel of 30-mm diameter. The particles were accelerated tangentially toward the plasma. Since the PMMA particles tend to agglomerate and partly stick to the cogwheel the accelerator produced showers of projectiles with a relatively broad velocity and size distribution. A vertical section through the dust cloud between the electrodes was illuminated by a thin sheet of laser light. The scattered light by the dust particles was observed at right angle with a CMOS camera at a frame rate of 97 fps. The field of view (FOV) of the camera is marked in Fig. 1.

<sup>\*</sup>arp@physik.uni-kiel.de

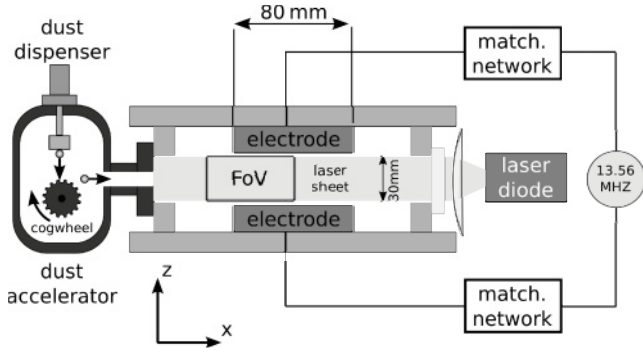


FIG. 1. Side view of the IMPF-K2 chamber. Particles are illuminated by a laser diode. The camera's field of view (FoV) is marked by a rectangle. Both electrodes are driven in push-pull mode by one rf generator via two matching networks.

### III. OBSERVATIONS

A still image of the dust cloud is shown in Fig. 2(a). The dust-free “void” region in the geometric center of the discharge is typical for dusty plasmas in parallel plate rf discharges under weightlessness conditions and is caused by radially outward streaming ions, which expel the dust from the center of the discharge [7]. The interparticle distance in the cloud was in the range  $b = (330\text{--}430) \mu\text{m}$ . A projectile from the dust accelerator enters the field of view from the left-hand side and moves through the dust cloud on a slightly upward-bent trajectory into the direction of the arrow. In the wake of the projectile a dust-free cavity is formed [see the dashed rectangle in Fig. 2(a)], which is magnified in Fig. 2(b). The elongated shape of the projectile is a consequence of the particle motion during the exposure of the video frame. In the presented snapshot the projectile has a velocity of  $v \approx 0.12 \text{ ms}^{-1}$ , which corresponds to a Mach number  $M = v/c_0 \approx 6$ , when a sound speed  $c_0 = 20 \text{ mm s}^{-1}$  is assumed, that is consistent with investigations of dust-density waves in the present chamber under similar conditions [13]. The cavity has a length of approximately 15 mm and a maximum diameter of  $\approx 1.0 \text{ mm}$ , which is reached  $\approx 5 \text{ mm}$  behind the projectile. The trajectory of the projectile is marked by the white solid curve in Fig. 2(b). As a consequence of the curved trajectory, the cavity is slightly asymmetric.

Two examples of other projectiles are presented in Figs. 2(c) and 2(d), which were observed in different video frames of the same experiment. A slow projectile ( $M \approx 0.8$ ) is shown in Fig. 2(c). It has a much shorter but wider cavity compared to the projectile in Figs. 2(a) and 2(b) with a maximum diameter of  $\approx 1.4 \text{ mm}$  approximately  $\approx 0.6 \text{ mm}$  behind the projectile. Figure 2(d) shows a fast projectile ( $M \approx 27$ ) which appears as bright streak above the white arrow due to its motion during the exposure of the video frame. In contrast to the previous projectiles, no pronounced cavity is observed. The presented experimental data is only one sample of a large number of observed events with a widespread range of projectile sizes and velocities. The presented observations are typical for all observed events.

Since the projectiles are subject to gas friction, plasma-induced forces, and possibly residual gravity, they move generally neither with constant velocity nor along a straight

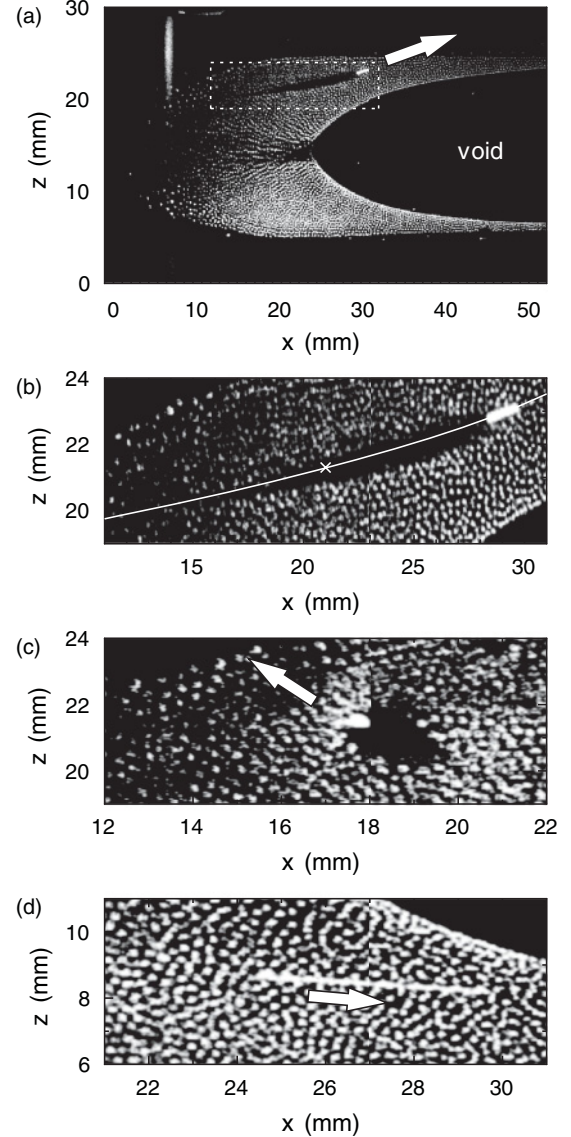


FIG. 2. (a) Vertical section through the dust cloud. The dust-free void region marks the center of the discharge. A projectile in the dashed rectangle moves through the dust cloud into the direction of the arrow (Mach number  $M \approx 4$ ). (b) Magnified view of the dashed region of interest in Fig. 2(a). The trajectory of the projectile is marked by the solid line. (c) Magnified view of a slow projectile ( $M \approx 0.8$ ) and (d) a fast projectile ( $M \approx 27$ ) in different video frames of the same experiment.

trajectory. As an example, Fig. 3 shows the temporal evolution of the horizontal ( $v_x$ , circles) and vertical ( $v_z$ , squares) velocity component of the projectile in Figs. 2(a) and 2(b). The horizontal velocity component decreases from  $v_x = 0.28 \text{ ms}^{-1}$  ( $M \approx 14$ ) when entering to  $v_x = 0.08 \text{ m s}^{-1}$  ( $M \approx 4$ ) at exiting the dust cloud. The exponential fit to  $v_x$  (solid curve) yields an effective friction coefficient  $\beta_p = 7.6 \text{ s}^{-1}$ . The good agreement between the fit and the data suggest that the horizontal motion of the projectile is dominated by a ballistic motion against gas friction and that plasma-induced forces are negligible since their topology would cause significant deviations from the observed exponential deceleration. The situation differs, for the motion in the vertical direction, since

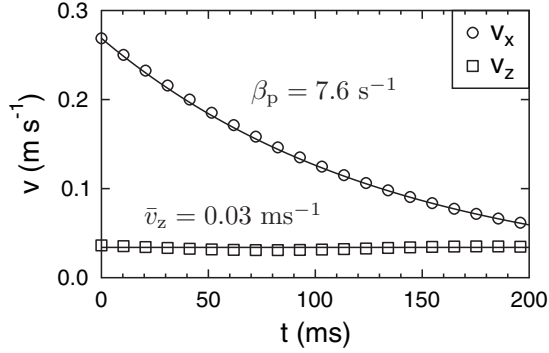


FIG. 3. Temporal evolution of the horizontal ( $v_x$ , circles) and vertical ( $v_z$ , squares) projectile velocity between entering ( $t = 0$ ) and leaving the dust cloud of the projectile shown in Figs. 2(a) and 2(b). The solid line is an exponential fit to  $v_x$  yielding an effective friction coefficient  $\beta_p = 7.6 \text{ s}^{-1}$ . The projectile moves in vertical direction with almost constant velocity of  $\bar{v}_z = 0.03 \text{ ms}^{-1}$ .

the projectile received almost no initial momentum in the vertical direction from the dust accelerator. Consequently, the slow vertical motion of the projectile is dominated by plasma-induced forces, i.e., the electric field force and the ion-drag force, as well as possibly residual gravity. Accordingly, the nearly constant vertical velocity of  $\bar{v}_z \approx 0.03 \text{ m s}^{-1}$  (horizontal line in Fig. 3) can be interpreted as the terminal velocity in an equilibrium between plasma-induced forces and gas friction. The effect of plasma induced-forces on the trajectory increases with decreasing projectile velocity. Consequently, fast projectiles [Fig. 2(d)] show a pure ballistic motion against gas friction, whereas slow projectiles [Fig. 2(c)] are drifting through the target cloud governed by plasma-induced forces. In the intermediate velocity regime [Fig. 2(a) and 2(b)], the projectile shows a significant deceleration due to gas friction while the influence of the plasma-induced forces grows, which causes the upward-bent trajectory in Fig. 2(b).

#### IV. LANGEVIN DYNAMICS SIMULATIONS

Langevin dynamics simulations of a three-dimensional dust cloud in a cylindrical flat-bottom harmonic confinement were performed containing 20 000 particles of the same radius and mass as in the experiment. The interaction between the particles in a dusty plasma is described by a shielded Coulomb (Yukawa) potential  $\phi(r) = (q_{t,p}/r) \exp(-r/\lambda_D)$  [14], where  $q_{t,p}$  is the charge of the target particle or the projectile, respectively, and  $\lambda_D$  the Debye screening length. Based on plasma simulations [15] of the present discharge and measurements under similar conditions [16] we choose  $\lambda_D = 385 \text{ }\mu\text{m}$  and  $q_t = -10^4 e$ . The simulation adds random motion to the particles, which corresponds to a kinetic temperature of  $T = 300 \text{ K}$  in an undisturbed system. Under these conditions the simulated dust cloud has an average dust density of  $n_d \approx 1.6 \times 10^{10} \text{ m}^{-3}$  in its central part ( $r < 2.5 \text{ mm}$ ,  $|z| < 5 \text{ mm}$ ) and an interparticle distance  $b = 423 \text{ }\mu\text{m}$ , which is in good agreement with the experiment. A projectile with a charge of  $q_p = -2 \times 10^5 e$  and a mass of  $m_p = 4.8 \times 10^{-11} \text{ kg}$  moves with an initial velocity of  $v_{z,0} = 0.3 \text{ m s}^{-1}$  starting at  $(r, z) = (0, -15) \text{ mm}$  in positive  $z$  direction. Both the projectile and

the target particles are subject to gas friction. The friction coefficient of the projectile  $\beta_p = 7.6 \text{ s}^{-1}$  was derived from the experiment, and the corresponding value for the target particles  $\beta_t = 37 \text{ s}^{-1}$  was calculated for the experimental conditions from Epstein's formula [17]. The projectile motion is radially constrained to  $r = 0$ . The parameters of the simulation were carefully chosen in order to achieve a good agreement with the projectile presented in Figs. 2(a) and 2(b). The temporal evolution of the projectile velocity in the simulation showed a deviation of less than  $1 \text{ mm s}^{-1}$  from the velocity measured in the experiment.

A projection of the dust cloud in the  $r$ - $z$  plane of cylindrical coordinates at  $t = 110 \text{ ms}$  is shown in Fig. 4(a). The solid contours visualize the confining potential in steps of  $0.2 \text{ V}$ . The position of the projectile is marked by a black dot on the  $z$  axis. Regions of different radial velocity distributions in the target cloud are separated by the dashed curves. In region I, inward and outward motion is equally distributed, whereas in regions II to IV the average motion of the target particles alternates between radially outward (II and IV) and inward (III) directed. The periphery of the target cloud is affected by confinement-induced shell formation, as found in other experiments [18] and simulations [19]. A pronounced cavity is formed in the wake of the projectile. From the boundary between regions I and II in Fig. 4(a) at the axial position of the projectile ( $z = 6.8 \text{ mm}$ ) one can conclude that the direct effect of the projectile on the target particles reaches up to  $\approx 2 \text{ mm}$  in radial direction, which is approximately 5 times the shielding length  $\lambda_D$ .

A spatiotemporal map of the radial velocity  $v_r$  at  $z = 0$  in the target cloud is shown in Fig. 4(b). The projectile passes the  $z = 0$  plane at  $t' = 0 \text{ ms}$ . One can clearly see a Mach cone structure with four to five nested cones of alternating direction of radial motion. Due to the strong damping in the system, the amplitude of the velocity fluctuations decays strongly with the radial distance from the trajectory of the projectile. At  $r > 1.5 \text{ mm}$  the absolute values of the radial velocity is significantly below  $1 \text{ mm s}^{-1}$ . The dashed line in Fig. 4(b) has a slope of  $c_0 = 25 \text{ mm s}^{-1}$ , which is in good agreement with the estimated sound speed of  $\approx 20 \text{ mm s}^{-1}$  in the experiment.

The temporal evolution of the cavity radius  $r_c$  at  $z = 0$  is plotted in Fig. 4(c). The radius is determined by finding the particle of minimal radial position in a thin slice of the dust cloud ( $|z| < 0.5 \text{ mm}$ ). Since the target particles are initially randomly distributed with respect to the future trajectory of the projectile the value  $r_c$  for  $t' < 0$  attains random values between  $0$  and  $b/2$ . When the projectile passes the  $z = 0$  plane  $r_c$  rapidly increases with an expansion velocity of  $v_{\text{exp}} \approx 45 \text{ mm s}^{-1}$  and reaches a maximum value  $r_{\text{max}} = 0.49 \text{ mm}$  at  $t'_{\text{max}} \approx 20 \text{ ms}$ . Then  $r_c$  decreases with almost constant velocity  $v_{\text{ret}} \approx -6.5 \text{ mm s}^{-1}$  and reaches a first minimum at  $t' \approx 85 \text{ ms}$  close to  $b/2$ . After a weak second expansion,  $r_c$  falls below  $b/2$  and decreases further, although much slower, for the rest of the time series. We attribute this complicated behavior of the cavity radius close to  $b/2$  to the interaction with the opposing cavity wall. Consequently, we consider the cavity closed, when  $r_c$  is close to  $b/2$ , especially when reaching the first minimum, or lower.

A more detailed analysis of the process of cavity closure allows the cylindrical distribution function (CDF), which is a measure for the probability of finding a target particle at

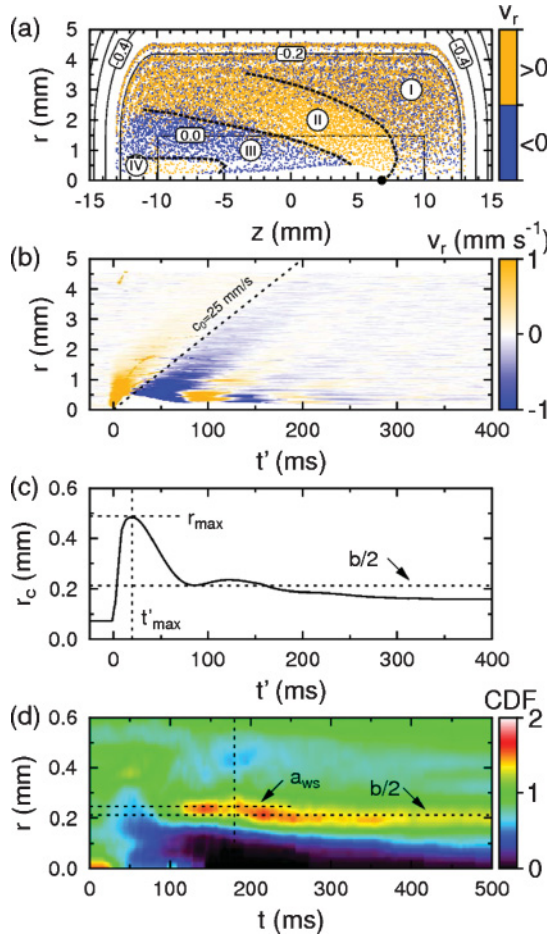


FIG. 4. (Color online) Langevin dynamics simulation of a cylindrical three-dimensional dust cloud containing 20 000 particles. (a) Projection of all particles into the  $r$ - $z$  plane of cylindrical coordinates at  $t = 110$  ms. The projectile (black dot on  $z$  axis) moves in positive  $x$  direction at  $r = 0$ . The dashed lines separate regions (I–IV) of different radial velocity distribution. The solid contours visualize the confining potential in steps of 0.2 V. (b) Spatiotemporal map of the radial velocity at  $z = 0$ . (c) Temporal evolution of the cavity radius. (d) Temporal evolution of the cylindrical distribution function (CDF) in the vicinity of the trajectory.

a radial distance  $r$  averaged over all axial positions  $z$ . The temporal evolution of the CDF is color coded in Fig. 4(d). At the beginning of the simulation ( $t = 0$  ms), target particles are found at every radial position. With increasing time the projectile expels target particles from small radial positions. When the first target particles close the cavity ( $t > 100$  ms) behind the projectile on the left-hand side of the cloud a sharp peak in the CDF emerges at a radial position that coincides with the Wigner-Seitz radius  $a_{ws} = [3/(4\pi n_d)]^{1/3} = 246 \mu\text{m}$ . The peak indicates a symmetric alignment of target particles with respect to the trajectory. The projectile leaves the dust cloud at  $t = 180$  ms [vertical dashed line in Fig. 4(d)] and a dust-free channel of  $\approx 0.1$  mm radius penetrates the complete cloud. The peak in the CDF moves subsequently to the smaller radial position  $b/2$  which suggests transition from a predominantly circular alignment to a hexagonal alignment of the target particles with respect to the trajectory of the projectile. With increasing time the radius of the dust-free

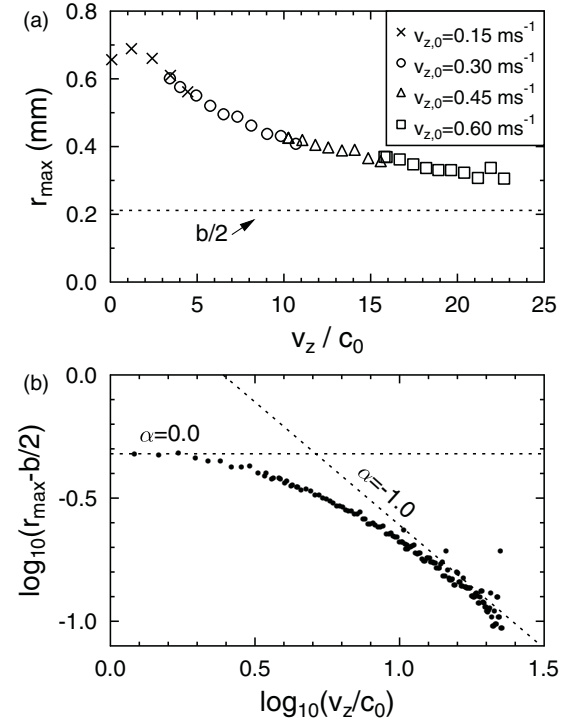


FIG. 5. Dependence of the maximum cavity radius  $r_{\text{max}}$  on the projectile velocity in linear (a) and double logarithmic (b) presentation.

channel gradually decreases due to a realignment of target particles as a consequence of diffusive (thermal) motion. We have verified that the observed alignment of target particles with respect to the trajectory of the projectile is not an artifact of the constrained projectile motion in the presented simulation.

In the following the effect of the projectile velocity on the cavity dynamics will be studied. The dependence of the maximum cavity radius  $r_{\text{max}}$  on the projectile velocity in units of  $c_0 = 25 \text{ mm s}^{-1}$  is plotted in Fig. 5(a). The figure contains the results of multiple simulations of the same target cloud and projectile as previously presented but with different initial projectile velocities  $v_{z,0} = (0.15\text{--}0.60) \text{ m s}^{-1}$ . In each simulation the maximum cavity radius was determined at different axial positions ( $z$ ), which correspond to different projectile velocities, as a consequence of its deceleration due to gas friction. Accordingly,  $r_{\text{max}}$  has a maximum value of almost 0.7 mm in the low velocity limit ( $v_z/c_0 < 1$ ) and decreases significantly with increasing projectile velocity. To study the dependence of the maximum cavity radius on the projectile velocity in more detail, Fig. 5(b) compiles the simulation data in a log-log plot. We consider only the case  $(r_{\text{max}} - b/2) > 0$ , because the previous observations revealed that the cavity dynamics at radii below  $b/2$  deviates significantly since it is governed by different processes. Obviously, the data do not follow a simple power law  $(r_{\text{max}} - b/2) \propto (v_z/c_0)^\alpha$ . Instead,  $r_{\text{max}} - b/2$  is almost constant, i.e.,  $\alpha = 0$ , for slow projectiles ( $v_z/c_0 < 2$ ) and it is proportional to  $(v_z/c_0)^{-1}$  at high velocities. The latter dependence suggests that the interaction between the projectile passing by a target particle

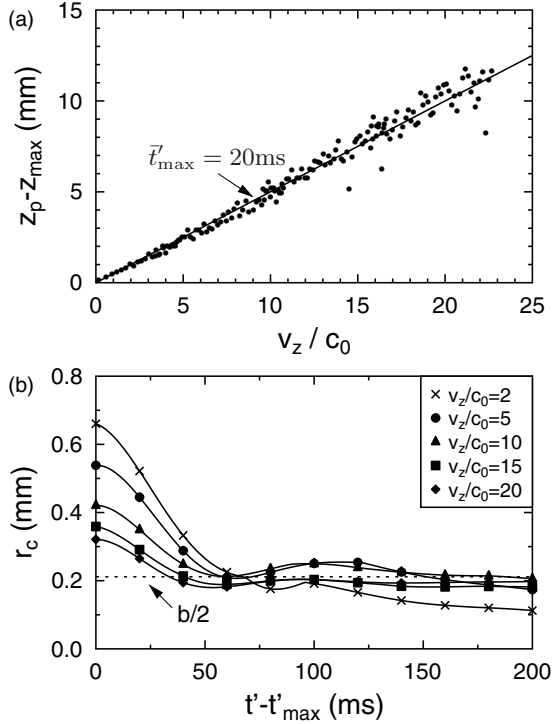


FIG. 6. (a) Axial position of maximum cavity expansion  $z_{\max}$  with respect to the position of the projectile  $z_p$  in dependence of the projectile velocity. (b) Temporal evolution of cavity closure for different projectile velocities.

is determined by a fixed interaction length if the projectile velocity is high enough.

A second important quantity that characterizes the opening process of the cavity is the axial position  $z_{\max}$  of the maximum cavity radius, with respect to the position of the projectile  $z_p$ . Figure 6(a) shows the dependence of  $z_p - z_{\max}$  on the projectile velocity  $v_z/c_0$ . Obviously,  $z_p - z_{\max}$  increases linearly with the projectile velocity, which implies that the cavity reaches its maximum expansion after a fixed time interval  $t'_{\max}$  after the passage of the projectile at a selected position. The solid line Fig. 6(a) is a linear fit to the data that yields  $\bar{t}'_{\max} \approx 20$  ms.

Differing from the opening process of the cavity, the time required to close the cavity is not constant. This finding is illustrated in Fig. 6(b), which shows the temporal evolution of the cavity radius  $r_c$  after reaching its maximum value for different values of  $r_{\max}$ , corresponding to different projectile velocities  $v_z/c_0 = 2 - 20$ . As earlier mentioned, the cavity closure shows a complex dynamical behavior when reaching small radii close to  $b/2$  or lower. This makes it difficult to quantify reliably the time required to close the cavity. Under the present conditions, a feasible measure is the time required to reach the first minimum of the cavity radius. Figure 6(b) reveals that it decreases obviously with the maximum cavity radius, i.e., cavities of smaller radius require less time to close than cavities of larger radius.

In order to compare the cavity shape in the simulation with the experimental data, Fig. 7 shows the intensity evolution perpendicular to the projectile trajectory in successive video frames at the cross mark in Fig. 2(b). The bright area

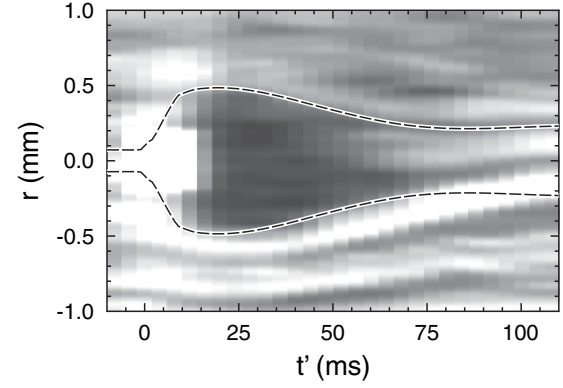


FIG. 7. Spatiotemporal map of the image intensity in Fig. 2(a) perpendicular to the trajectory of the projectile at the cross mark in Fig. 2(b). The two dashed curves indicate the cavity radius obtained from the simulation.

surrounding  $(r, t) = (0, 0)$  corresponds to the projectile. The dashed curves indicate the temporal evolution of the cavity radius  $r_c$  in the simulation. The simulation shows an excellent agreement in shape and size of the cavity with the experiment. The asymmetry of the experimental cavity shape for  $t > 50$  ms can be attributed to the slightly curved trajectory of the projectile. The only free parameter in the simulation is the projectile charge, which was determined from a fit to the experimental cavity radius. The simulation revealed that the maximum cavity radius increases with the projectile charge. A detailed investigation of this dependency will be subject of future investigations. The resulting value of the projectile charge  $q_p = -2 \times 10^5 e$  corresponds to an agglomerate of a few (10) PMMA particles, which is reasonable, when comparing the visual appearance of the projectile with a single PMMA particle in the plasma. Although the spatial resolution of the experimental data is not sufficient to reliably resolve a particle alignment after the cavity has closed, one can clearly see a stripe of reduced intensity close to  $r = 0$ , which supports the result of the simulation.

## V. DISCUSSION AND CONCLUSION

Our investigations show that a supersonic projectile that penetrates a dusty plasma generates a dust-free cavity in its wake whose expansion and relaxation dynamics happen on significantly different time scales. It was found that the cavity shape strongly depends on the projectile velocity. Very slow projectiles were surrounded by an almost spherical cavity. With increasing projectile velocity the cavity becomes more and more elongated while its maximum radius decreases. Since the exact size and therefore the charge of the projectile is unknown in the experiment, it is not possible to compare the different observed projectiles quantitatively. Nevertheless, deceleration of a projectile due to gas friction allows verification of the validity of the above statements by observing single projectiles at different velocities.

The much better spatiotemporal resolution of the simulation compared to the experiment allowed to identify three major phases in the complex dynamics of the cavity: First, the expansion phase, in which the cavity increases until its

maximum value is reached. In contrast to the maximum cavity radius the duration of the expansion phase is independent of the projectile velocity. Consequently, the distance along the trajectory between the projectile and the position of maximum cavity radius increases linearly with the projectile velocity. The second phase of the cavity dynamics is the contraction phase. The end of the phase is not well defined, since the cavity shows a complicated behavior when approaching radii close to  $b/2$ . At the selected simulation parameters, the cavity radius reaches typically a first minimum close to  $b/2$ , increases slightly again, and falls finally below  $b/2$ . This “overshoot” can be attributed to the interaction with the opposing cavity wall and is also visible when inspecting the raw video data of the experiment. It was found that the time interval from the beginning of the contraction phase to the first minimum of the cavity radius decreases with the maximum cavity radius  $r_{\max}$ . Since in our simulation the different values of  $r_{\max}$  are a consequence of different projectile velocities, the presented data does not allow us to exclude a direct dependency of the projectile velocity on the duration of the contraction phase. However, we hypothesize that the time required to close the cavity is defined by  $r_{\max}$  and the viscoelastic-properties of the target cloud rather than by the projectile velocity.

Although the cavity has closed after the second phase, the target cloud is still affected by the previous processes. In the final phase, the target particles realign in the target cloud. The penetration by the projectile caused the target cloud to align symmetrically with respect to the trajectory of the projectile, which results in a dust-free channel in the target cloud. It was found that the channel is stable for several hundred milliseconds, which is much longer than the duration of the first two phases of the cavity dynamics. Similar to the channeling effect in solid crystals [20] the observed phenomenon is expected to play an important role for lane

formation [21] in a dusty plasma. Further, we expect that the kinetic temperature of the dust particles, i.e., their thermal random motion, is a crucial parameter for the stability of the channel.

The presented simulations consider only one value for the projectile charge which was determined by best fit to the experiment. A larger projectile charge in the simulation results in a larger maximum cavity radius. Also the properties of the target cloud, i.e., particle density and charge, the shielding length of the plasma as well as the gas friction affect the value of  $r_{\max}$  and the time scales of the cavity dynamics. A detailed study of the effect of these quantities on the cavity dynamics requires comprehensive additional simulations.

The interaction between the projectile and the target cloud is not limited to the region of the cavity but reaches far into the dust cloud, which results in the formation of nested cones of alternating direction of radial motion. This structure is the three-dimensional analog of the phonon wake [22] behind a moving distortion in a two-dimensional dusty plasma.

Our simulations revealed a multitude of interesting features regarding the interaction between fast projectiles with a dusty plasma. To allow a systematic comparison with the experiment and to identify the fundamental physical mechanisms that cause the complex cavity dynamics additional simulations and refined experiments with well-defined projectile sizes and high-resolution particle tracking are planned for near future.

#### ACKNOWLEDGMENTS

This work was supported by the German aerospace agency (DLR) under Grant No. 50WM0739/50WM1139 and by the European Space Agency (ESA). The authors thank K. O. Menzel for helpful discussions. The expert technical assistance by V. Rohwer and M. Poser is gratefully acknowledged.

- 
- [1] F. Hoerz *et al.*, *Science* **314**, 1716 (2006).
  - [2] E. G. Richardson, *Proc. Phys. Soc. London* **61**, 352 (1948).
  - [3] B. Akers and A. Belmonte, *J. Non-Newtonian Fluid Mech.* **135**, 97 (2006).
  - [4] J. W. J. de Folter, V. W. A. de Villeneuve, D. G. A. L. Aarts, and H. N. W. Lekkerkerker, *New J. Phys.* **12**, 023013 (2010).
  - [5] D. Lohse, R. Bergmann, R. Mikkelsen, C. Zeilstra, D. van der Meer, M. Versluis, K. van der Weele, M. van der Hoef, and H. Kuipers, *Phys. Rev. Lett.* **93**, 198003 (2004).
  - [6] H. Rothermel, T. Hagl, G. E. Morfill, M. H. Thoma, and H. M. Thomas, *Phys. Rev. Lett.* **89**, 175001 (2002).
  - [7] G. E. Morfill, H. M. Thomas, U. Konopka, H. Rothermel, M. Zuzic, A. Ivlev, and J. Goree, *Phys. Rev. Lett.* **83**, 1598 (1999).
  - [8] D. Samsonov, J. Goree, Z. W. Ma, A. Bhattacharjee, H. M. Thomas, and G. E. Morfill, *Phys. Rev. Lett.* **83**, 3649 (1999).
  - [9] A. Melzer, S. Nunomura, D. Samsonov, Z. W. Ma, and J. Goree, *Phys. Rev. E* **62**, 4162 (2000).
  - [10] K. Jiang *et al.*, *Europhys. Lett.* **85**, 45002 (2009).
  - [11] C. O. Thompson, N. D’Angelo, and R. L. Merlino, *Phys. Plasmas* **6**, 1421 (1999).
  - [12] M. Klindworth, O. Arp, and A. Piel, *J. Phys. D: Appl. Phys.* **39**, 1095 (2006).
  - [13] A. Piel, O. Arp, M. Klindworth, and A. Melzer, *Phys. Rev. E* **77**, 026407 (2008).
  - [14] M. Lampe, G. Joyce, G. Ganguli, and V. Gavrishchaka, *Phys. Plasmas* **7**, 3851 (2000).
  - [15] SIGLO-2D, Version 1.1, Kinema Software.
  - [16] M. Klindworth, O. Arp, and A. Piel, *Rev. Sci. Instrum.* **78**, 033502 (2007).
  - [17] P. S. Epstein, *Phys. Rev.* **23**, 710 (1924).
  - [18] O. Arp, D. Block, A. Piel, and A. Melzer, *Phys. Rev. Lett.* **93**, 165004 (2004).
  - [19] M. Bonitz, D. Block, O. Arp, V. Golubnychiy, H. Baumgartner, P. Ludwig, A. Piel, and A. Filinov, *Phys. Rev. Lett.* **96**, 075001 (2006).
  - [20] G. R. Piercy, F. Brown, J. A. Davies, and M. McCargo, *Phys. Rev. Lett.* **10**, 399 (1963).
  - [21] K. R. Sütterlin *et al.*, *Phys. Rev. Lett.* **102**, 085003 (2009).
  - [22] D. H. E. Dubin, *Phys. Plasmas* **7**, 3895 (2000).